Proceedings of the Thirty-sixth (2026) International Ocean and Polar Engineering Conference
Orlando, Florida, USA, May 31-June 5, 2026

ISBN 978-1-880653-72-2; ISSN 1098-6189

www.isope.org

Numerical Study on the Mechanism of Underwater Fluctuating Pressure Induced by Vortex Shedding from a Vertical Cylinder

*Lianjie Yu[1], Qi Shen[1], Jin Liu[1], Decheng Wan[2]**

[1] China Ship Scientific Research Center, Wuxi, China
[2] Computational Marine Hydrodynamics Lab (CMHL), School of Ocean and Civil Engineering, Shanghai Jiao Tong University, Shanghai, China
*Corresponding author

ABSTRACT

In civil and military facilities, cylinder bodies are applied in various underwater orientations. Pressure fluctuations on the cylinder surface constitute a critical acoustic source for hydrodynamic noise. This paper focuses on vertical cylinders as the research object, conducting numerical simulations under different diameter conditions. Structured grids are employed to enhance computation accuracy. After validating the numerical results, the study established a flow-acoustic correlation by analyzing wake flow field at different Reynolds numbers, thereby explaining variations in pressure fluctuation at different locations. The results indicate that higher flow velocities and larger diameters lead to larger vortex scales and increased overall pressure levels. Additionally, the cylinder's inclination angle affects velocity distributions.

KEY WORDS: Pressure fluctuation, vertical cylinder, vortex shedding, DES.

INTRODUCTION

Cylindrical configurations are common fundamental geometric structures in underwater acoustic detection systems, such as pillar-mounted sonar and towed array sonar (Sean, 2019).

Many scholars consider pressure fluctuation as the primary noise source, making its study on towed body surfaces a key research focus. Due to their high length-to-diameter ratio, such objects cannot undergo physical wind tunnel experiments and must be tested at sea or on lakes. Numerical simulations also provide a viable research pathway. For instance, Tutty (2008) simulated flows around axial cylinders with varying diameters, covering Reynolds numbers from 6,203 to 92,310. Jordan conducted similar simulations of axial cylinder flows and derived a semi-empirical formula for friction coefficients. Karthik (2020) performed CFD simulations on slender cylinders at speeds ranging from 2 to 5 knots, revealing a ~5% discrepancy in the boundary layer shape factor compared to flat plate flows.

The research on flow around cylinders is categorized into zero-attack-angle flow and angled-attack flow. Traditionally, zero-attack-angle boundary layer flows were considered analogous to flat plate flows. However, extensive experiment and numerical studies by the Naval Undersea Warfare Center (NUWC) demonstrated that the boundary layer characteristics deviate from those of flat plates when the TBL thickness exceeds the cylinder radius.

Angled-attack flow around a cylinder constitutes a classic flow-around-body problem. Flow-around bodies are categorized into smooth bodies, for example, cylinders, whose separation points vary with flow velocity, and angular bodies, for instance, square cylinders, where separation points are fixed at corner points. In cylinder flow, a velocity difference exists between the boundary layer and the free stream, forming a shear layer. The asymmetry in shear layers on both sides of the cylinder generates regular vortex shedding in the wake region. As early as the 19th century, Strouhal discovered that the vortex shedding frequency is proportional to the flow velocity and inversely proportional to the cylinder diameter.

Generally, end vortices of three-dimensional cylinders influence the wake vortex behavior, leading to higher drag and lift coefficients in 2D cylinders compared to 3D cases. This study employs a 2D cylinder, which may introduce minor errors in drag and lift measurements but does not affect the analysis of pulsating characteristics.

This paper investigates fluctuating pressure on cylinder structures, including vertical and inclined cylinder configurations. Numerical simulations are conducted for cylinders with diameters of 25 mm, 35 mm, 45 mm, and 66 mm, under incoming flow velocities of 1.5, 3, 4.5, 6, 7.5, and 9 m/s. After validating the simulated results against experiment peak frequency, spatial characteristics of fluctuating pressure distributions are analyzed.

Flow Field Simulation Method

For most deep water conditions, the effect of free surface can be neglected. The compressibility can be ignored for underwater low-speed motion. Based on assumptions such as the continuum hypothesis of fluid and the generalized Newton's law of internal friction, the incompressible Navier-Stokes equations for underwater flow can be derived, which take the form:

$$\frac{Du_1}{Dt} = f_1 - \frac{1}{\rho}\frac{\partial p}{\partial x_1} + \nu\nabla^2 u_1$$
$$\frac{Du_2}{Dt} = f_2 - \frac{1}{\rho}\frac{\partial p}{\partial x_2} + \nu\nabla^2 u_2$$
$$\frac{Du_3}{Dt} = f_3 - \frac{1}{\rho}\frac{\partial p}{\partial x_3} + \nu\nabla^2 u_3$$

here, u_1, u_2, and u_3 represent the velocity components in the x_1, x_2, and x_3 directions respectively. ρ denotes the water density, p denotes the dynamic pressure of water, and ν denotes the kinematic viscosity coefficient. $\frac{D}{Dt} = \frac{\partial}{\partial t} + \vec{u} \cdot \nabla$ represents the material derivative operator. f_1, f_2, and f_3 are the specific external forces (per unit mass) acting in the x_1, x_2, and x_3 directions, such as gravitational force.

For the numerical solution of the Navier-Stokes equations, there are two primary approaches: the first decomposes variables in the temporal scale, splitting velocity into time-averaged and fluctuating components (Reynolds decomposition); the second decomposes variables in the spatial scale, separating velocity into large-scale quantities (resolvable scales) and subgrid-scale quantities. The former is termed the Reynolds-Averaged Navier-Stokes (RANS) method, whose drawback is its inability to accurately account for turbulent fluctuations. The latter is called the Large Eddy Simulation (LES) method, whose limitation is its extremely high computational cost. The Detached Eddy Simulation (DES) method, which combines both approaches, has emerged as a more practical computational tool for engineering applications.

The DES method is employed in this paper, which balances computational accuracy and efficiency effectively for fluctuating pressure computation.

Frequency Spectrum Analysis Method

The Fourier transform can convert any function into a sum of trigonometric functions with different periods. Assuming this arbitrary function is an *n*-th degree polynomial, the form of the polynomial function can be determined uniquely, as long as n+1 pairs of the polynomial's independent variable and dependent variable are provided. The method of determining an *n*-th degree polynomial using *n*+1 pairs of values is called the point-value representation.

Assuming a polynomial of degree *n* is split into two parts based on the parity of the indices of its coefficients.

$$f(x) = (a_0 + a_2x^2 + \cdots + a_{n-2}x^{n-2}) + (a_1x + a_3x^3 + \cdots + a_{n-1}x^{n-1})$$

Let

$$f_1(x) = \left(a_0 + a_2x^1 + \cdots + a_{n-2}x^{\frac{n}{2}-1}\right)$$

$$f_2(x) = \left(a_1 + a_3x^1 + \cdots + a_{n-1}x^{\frac{n}{2}-1}\right)$$

Assuming the roots on the unit circle are divided into *n* parts equally, the complex number with the smallest positive argument is ω, then

$$\omega_n = \cos\frac{2\pi}{n} + i\sin\frac{2\pi}{n}$$

According to Euler's formula, we have

$$\omega_n^k = \cos\frac{2k\pi}{n} + i\sin\frac{2k\pi}{n}$$

Substituting $x = \omega_n^k$ $(k < \frac{n}{2})$ into $f(x)$, we get

$$f(\omega_n^k) = f_1(\omega_n^{2k}) + \omega_n^k f_2(\omega_n^{2k})$$

Substituting $x = \omega_n^{k+\frac{n}{2}}$ $(k < \frac{n}{2})$ into it, we get

$$\begin{aligned} f\left(\omega_n^{k+\frac{n}{2}}\right) &= f_1(\omega_n^{2k+n}) + \omega_n^{k+\frac{n}{2}} f_2(\omega_n^{2k+n}) \\ &= f_1(\omega_n^{2k} \cdot \omega_n^n) - \omega_n^k f_2(\omega_n^{2k} \cdot \omega_n^n) \\ &= f_1(\omega_n^{2k}) - \omega_n^k f_2(\omega_n^{2k}) \\ &= f_1\left(\omega_{\frac{n}{2}}^k\right) - \omega_n^k f_2\left(\omega_{\frac{n}{2}}^k\right) \end{aligned}$$

Based on the two equations above, it can be observed that knowing $f_1\left(\omega_{\frac{n}{2}}^k\right)$ and $f_2\left(\omega_{\frac{n}{2}}^k\right)$ allows us to determine all other values. To find $f_1\left(\omega_{\frac{n}{2}}^k\right)$ and $f_2\left(\omega_{\frac{n}{2}}^k\right)$, we can use $f_1\left(\omega_{\frac{n}{4}}^k\right)$ and $f_2\left(\omega_{\frac{n}{4}}^k\right)$... following this pattern, the problem ultimately reduces to solving for

$$f_1(\omega_1^k) = f_2(\omega_1^k) = 1$$

By applying the recursive divide-and-conquer approach repeatedly, this solving process is termed the "butterfly transformation". It accelerates the computation of the discrete Fourier transform (DFT) significantly, hence the name "fast Fourier transform" (FFT).

When applying FFT, there may be individual data points with deviations in the signal, which can lead to large variance in the resulting frequency spectrum. To address this issue, this paper adopts the Welch's modified periodogram method. The specific procedure involves:

(1) Selecting an appropriate window function, which is applied prior to computing the periodogram.

(2) Segmenting the data with overlapping sections—when segments are allowed to overlap, the variance of the estimate decreases. Research has shown that the variance is minimized when the overlap ratio is 0.5.

(3) After obtaining the periodogram for each segment, the Welch correction function is applied to each to reduce spectral bias and noise. Finally, the modified periodograms are averaged to produce the final estimate.

Pressure Fluctuation Computation Method

Fluctuating pressure denotes the pressure variations on the object surface induced by disturbances in the turbulent boundary layer. It is defined as the difference between the instantaneous pressure and the time-averaged pressure quantitatively. The computation procedure for fluctuating pressure in CFD is outlined in Workflow 1.

Workflow 1：Pressure Fluctuation Computation Method	
1	Initialization: Define the set of probe locations *S* and adopt a fixed time step *Δt* for DES.
2	For all sensor locations, perform DES to obtain flow field variables (velocity, pressure, etc.) at each time *t*.
3	Record pressure data at intervals of *Δt* post-initialization and write in files.
4	Check pressure scaling and apply fluid density correction if required.
5	Terminate simulation and save pressure time-histories when sampling concludes.
6	Subtract time-averaged pressure from each sensor's time-history data to obtain pulsating pressure.
7	Apply Fourier transform to the pulsating pressure time-series to derive the pressure power spectral density.

When calculating underwater pressure fluctuation, it is critical to ensure the rationality of grid quality and time-step selection. Near-wall regions require unstructured grid refinement to enhance resolution, while time steps must satisfy the CFL stability criterion and be smaller than the minimum characteristic period of pressure fluctuations. For boundary conditions, non-reflective or periodic boundaries are adopted to minimize artificial reflections. Numerical algorithms should prioritize PISO or SIMPLEC schemes to improve transient stability, with residual thresholds strictly controlled (e.g., <1e-6) to reduce truncation errors.

Data sampling adheres to the Nyquist-Shannon theorem, combined with wavelet denoising to retain physical signal integrity. Accurate fluid property inputs and depth-dependent hydrostatic pressure corrections are essential. Finally, computational reliability is validated through grid independence analysis, temporal convergence tests, and experimental comparisons, ensuring precise quantification of pressure amplitude, frequency, and spatial distribution characteristics.

Vortex identification methods

Vortices are a critical manifestation of flow field complexity, tied to viscous fluid dynamics (Yu, et., 2021). The capability to capture vortex structures exemplifies the superiority of viscous flow solvers in CFD over potential flow solvers. Furthermore, vortices are intrinsically linked to underwater hydrodynamic noise sources and radiated noise generation. Thus, developing accurate vortex identification techniques is essential for elucidating the fluid-acoustic coupling mechanisms underlying such phenomena.

Vorticity characterizes the local rotation strength of fluid elements quantitatively, directly defining the intensity and spatial distribution in a flow field. A vortex, as a coherent rotational flow region, inherently manifests where the vorticity magnitude is significant, with its dynamics governed by the evolution of the vorticity field.

Mathematically, the curl of the velocity field yields the vorticity vector, whose magnitude and orientation specify the axis and rate of fluid rotation, forming the theoretical basis for identifying and analyzing vortex structures. Thus, vorticity serves as the essential mathematical descriptor linking the abstract concept of "vortices" to quantifiable fluid dynamics, enabling the analysis of their generation, advection, and dissipation in complex flows.

$$\boldsymbol{\omega} = \nabla \times \boldsymbol{V}$$

Vorticity (ω) is defined as the curl of the fluid velocity field, assuming fluid parcels obey rigid-body rotation. While mathematically rigorous, this framework neglects physical realities: real fluid motion deviates from idealized rigid-body dynamics, and the correspondence between structures in boundary layers and vorticity iso-surfaces remains physically questionable, as viscous effects and anisotropic flow behaviors invalidate such assumptions.

In 1988, Hunt proposed the Q criterion, marking the second revolution in viscous flow vortex identification. The criterion is defined by:

$$\mathrm{Q} = \frac{1}{2}(\|\boldsymbol{B}\|_F^2 - \|\boldsymbol{A}\|_F^2)$$

here, $\|\ \|_F$ denotes the Frobenius norm, and its square is equivalent to the sum of the squares of all matrix elements. Matrices $\boldsymbol{A}$ and $\boldsymbol{B}$ represent the symmetric and antisymmetric tensors of the velocity gradient, respectively.

$$\boldsymbol{A} = \frac{1}{2}(\nabla\boldsymbol{u} + \nabla\boldsymbol{u}^T)$$
$$\boldsymbol{B} = \frac{1}{2}(\nabla\boldsymbol{u} - \nabla\boldsymbol{u}^T)$$

The definition of the Q criterion indicates that when Q > 0, the rotational component dominates the fluid motion, whereas when Q < 0, the shear component prevails. While the Q criterion significantly enhances the physical interpretation of vortex structures compared to vorticity, it still has limitations. For instance, the spatial distribution and scale of vortex structures are highly sensitive to the chosen Q threshold; even when Q > 0, shear contamination may persist, generating spurious vorticity in shear-dominated flows.

VALIDATION OF SIMULATIONS

The computational domain for the vertical cylinder flow disturbance is shown in the figure below, with the viewing angle aligned along the z-axis direction. The freestream velocity is denoted as $\mathrm{U_0} = 1.5\mathrm{m/s}$, and the cylinder diameter D is set to 25 mm, 35 mm, 45 mm, and 66 mm respectively. The origin is located at the center of the inlet boundary. The computational domain has a streamwise length of 0.45 m and a spanwise length of 0.2 m, with the cylinder center positioned 0.05 m away from the inlet plane.

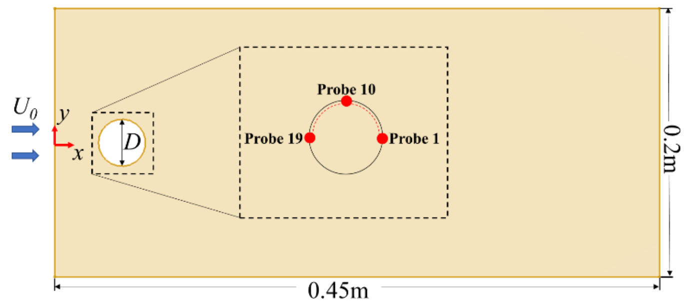

Fig. 1 Schematic diagram of the computation domain and pressure probe locations.

A no-slip wall boundary condition is applied on the cylinder surface, while the left and right sides use symmetry boundary conditions. The inlet face is set to a fixed velocity boundary condition, and the outlet is specified as a fixed pressure condition. To reduce computation cost, the domain length is minimized to 0.02 m in *z* direction with only 10 grid points. The two side boundaries in the z-direction are also defined as symmetry conditions to simulate an infinitely long configuration.

To monitor unsteady pressure fluctuation data, wall pressure probes are placed on the cylinder surface. Probes are positioned every 10° around the cylinder circumference and labeled as Probe 1 to Probe 19.

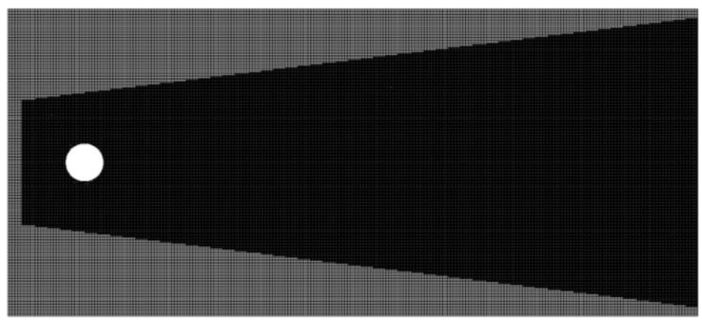

Fig. 2 Schematic of mesh in the wake region (coarser mesh).

Structured grids are employed as illustrated in the figure 2. This approach ensures mesh quality and guarantees the computational accuracy of subsequent unsteady pressure calculations. The total number of grids is 430,000, with 10 boundary layers added. The first-layer grid thickness is 1×10^{-4}m, and the stretching ratio is 1.05. The velocity-pressure decoupling is addressed using the PISO (Pressure-Implicit with Splitting of Operators) algorithm.

In the von Kármán vortex street in the cylinder wake, two alternating vortices with opposite rotation directions are shed from the cylinder in a regular pattern periodically. This shedding frequency f_s is proportional to the freestream velocity $\mathrm{U_0}$, and inversely proportional to the cylinder diameter *D*, i.e.,

$$f_s = \mathrm{St}\frac{U_0}{D}$$

The proportionality coefficient in the equation is the Strouhal number (St), which is dependent on the Reynolds number (Re). Based on experimental study (Stephen, 2014), the Strouhal number approaches a nearly constant value of 0.21 for Reynolds numbers exceeding 1000.

Table 1. Comparison of vortex shedding frequencies for a cylinder.

	Experiment	CFD
Strouhal number	0.210	0.240
Error	-	14%

The Fourier transform of the lift force time-history data on the cylinder surface yielded a first-mode peak frequency of approximately 14.4 Hz. The derived Strouhal number was compared with Roshko's experimental results (see Table 1), exhibiting discrepancies within acceptable error bounds, which validates the reliability of the computed fluctuating pressure.

THE CORRELTAION BETWEEN FLOW FIELD AND PRESSURE FLUCTUATION

The Effect of Velocity on Vortex Scale

The vorticity and Q criterion were applied to analyze the vortex distribution behind a cylinder under different flow velocities. Both methods yielded consistent results: vortex scale and energy increase with higher flow velocity, as Figure 3 and Figure 4 show.

The Q criterion and vorticity-based methods are two classical approaches for vortex identification. Vorticity quantifies local rotation via the velocity field's curl, offering computational efficiency and intuitive physical interpretation but limited precision for small-scale vortices and sensitivity to low-resolution grids. The Q criterion, defining vortices where the rotational component of the velocity gradient tensor exceeds strain-rate contributions, provides higher resolution for fine-scale structures but requires nonlinear threshold, incurs greater computational cost, and is noise-sensitive. While vorticity methods excel in speed and macroscopic feature capture, Q criterion better resolves complex flow details at the cost of parameter dependency. Their combined use is common: vorticity maps initial distributions, while Q criterion refines critical regions, with selection dictated by flow complexity and resource constraints.

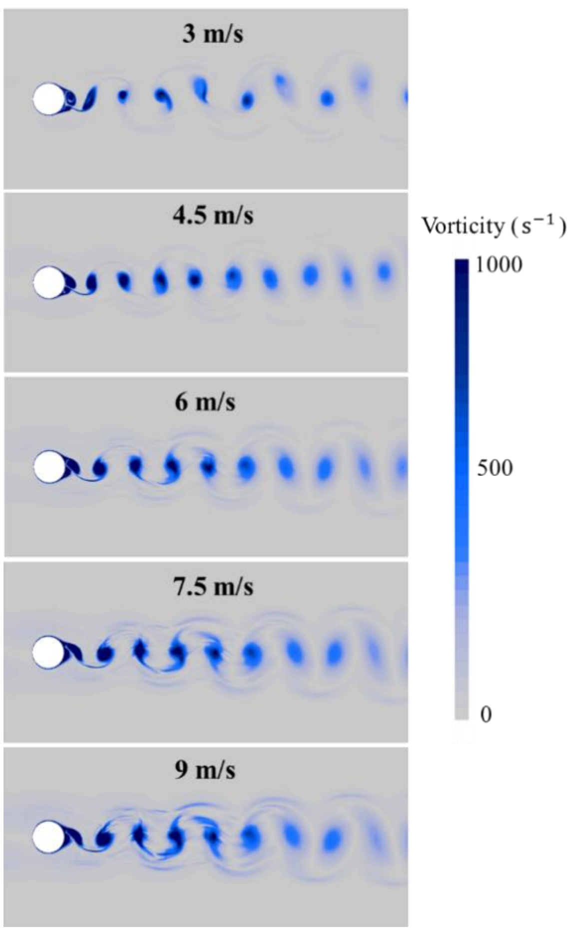

Fig. 3 Vorticity-based visualization of the wake vortex distribution.

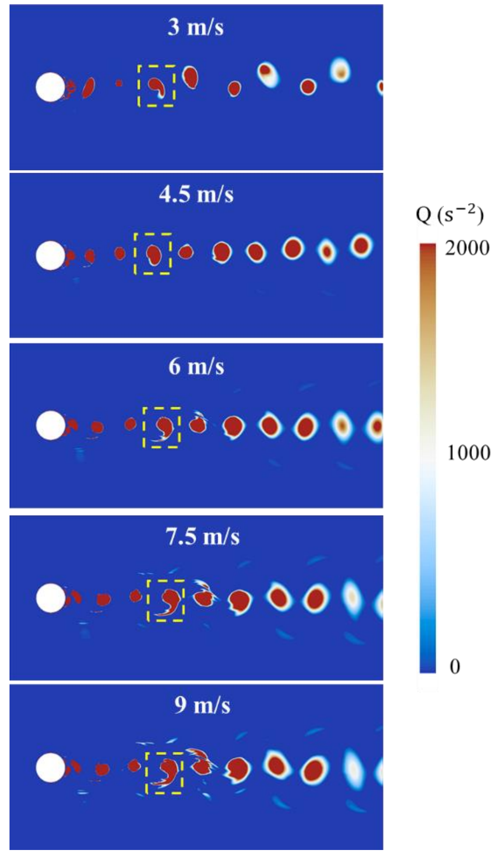

Fig. 4 Q-criterion-based wake vortex distribution

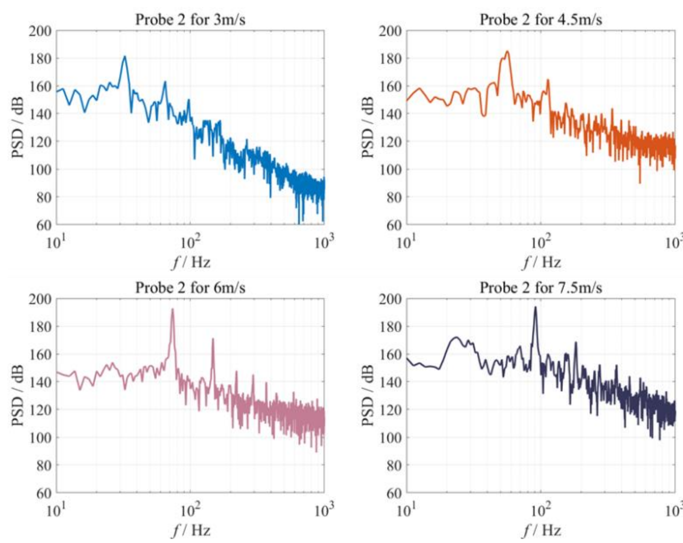

Fig. 5 Fluctuating pressure auto-spectrum at Probe 2 under different incoming velocities (D = 35 mm).

In cylinder flow, the enlargement of wake vortex scales with increasing inflow velocity stems from the altered balance between inertial and viscous forces primarily. As velocity rises, the Reynolds number increases, shifting the flow toward inertial dominance, which amplifies vortex generation and spatial expansion. Vortex kinetic energy, proportional to U^2, grows with velocity, directly driving spatial vortex expansion. At moderate Re, the Strouhal number remains approximately constant, necessitating spatiotemporal scale adjustments to conserve energy, thereby extending vortex dimensions with velocity. At high

Reynolds numbers, turbulence intensifies, enhancing randomness and interaction ranges, further enlarging vortex scales.

The fluctuating pressure auto-spectrum at Probe 2 is shown in Figure 5. It can be observed that as the flow velocity increases, the peak frequency gradually rises, and the amplitude of the first-order peak also increases. These findings align with both theoretical predictions and experiment results.

The Effect of Velocity on Vortex Scale

The Figure 6 shows instantaneous vorticity distribution contours of the vortex street for cylinders of different diameter. It can be observed that larger cylinder diameters result in broader vorticity distribution ranges. This explains why larger cylinder sizes lead to higher fluctuating pressure magnitudes, as Figure 7 shows.

The enlargement of Karman vortex street dimensions with increasing cylinder diameter stems from multiple interrelated mechanisms. First, the characteristic scales of vortices, such as core width and spacing, are directly proportional to the cylinder diameter due to the geometric dominance of the cylinder's dimensions in vortex formation. Second, the increased Reynolds number associated with larger diameters promotes turbulent flow transitions, delays boundary layer separation, and thickens shear layers, thereby amplifying vortex development. Third, the Strouhal number, which remains approximately constant within moderate Reynolds number ranges, results in lower vortex shedding frequencies as diameter increases, prolonging the shedding cycle and allowing vortices to expand spatially. Additionally, larger cylinders exhibit stronger "blockage effects" that increase boundary layer thickness and expand wake adjustment zones, further magnifying vortex dimensions. These combined factors—geometric scaling, Reynolds number dependence, Strouhal number constraints, and flow-blocking dynamics—collectively explain the observed increase in Karman vortex dimensions with cylinder diameter.

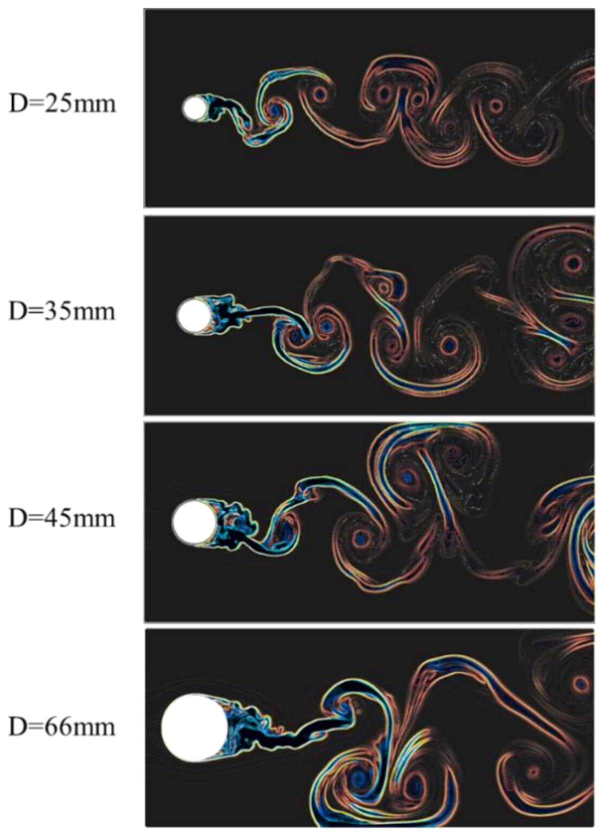

Fig. 6 The vortex shedding for different diameters ($U_0 = 1.5\mathrm{m/s}$).

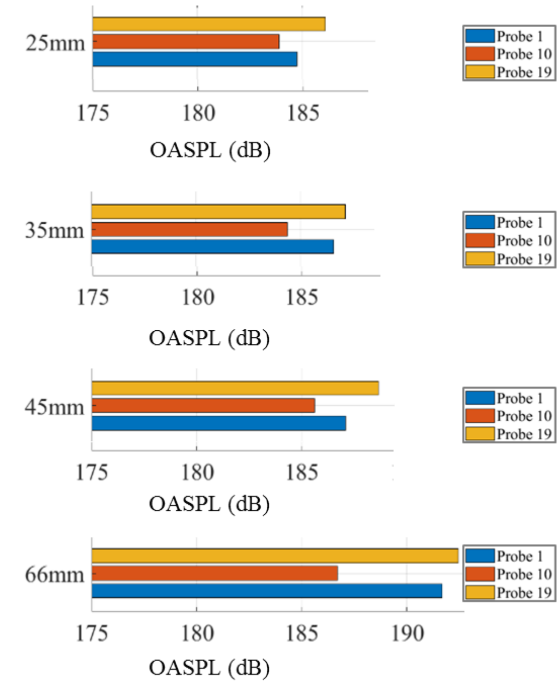

Fig. 7 The vortex shedding for different diameters ($U_0 = 1.5\mathrm{m/s}$).

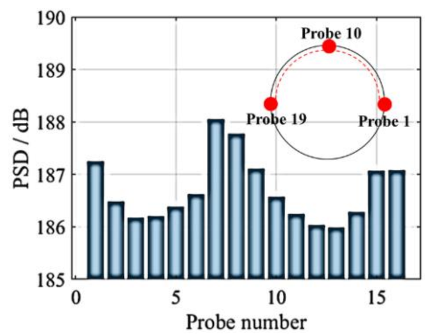

Fig. 8 Fluctuating pressure at different locations on the cylinder object surface.

To further analyze the pulsating pressure peak magnitudes at each probe location, the pulsating pressure peaks from Probe1 to Probe16 were extracted, as shown in Figure 8. The results indicate that the largest pressure peak (exceeding 188 dB) occurs at Probe7, corresponding to an inflow angle of 60°. Additionally, significant pressure peaks are also observed at the upstream (Probe 1) and downstream (Probe 16) positions of the cylinder.

Influence of Angle of Attack

The flow dynamics of a 60°-inclined cylinder configuration with 35mm diameter is selected as the inclined test case in this paper, with the computational domain illustrated in Figure 9.

The inclination (angle of attack) of a cylinder alters the vortex shedding flow field by disrupting the inherent periodicity of symmetric flow, transforming the traditional symmetric Karman vortex street into asymmetric skewed vortex patterns with distorted frequency characteristics and a deviation of the Strouhal number from its canonical constant value. This results in increased fluctuation amplitudes of lift and drag forces, while the migration of separation points induced by the angle exacerbates the asymmetry in pressure fluctuations. At large angles of attack, the flow may transition to unstable regimes or turbulent states due to destabilization of the vortex shedding process. These effects stem from the introduction of additional shear forces and separation point displacement caused by the angle, leading to asymmetric phase dynamics, vortex core scaling, and energy distribution in the flow field, thereby amplifying its complexity and structural vibration risks.

Fig. 9 Fluctuating pressure at different locations on the cylinder object surface.

The height-dependent velocity distribution in the wake region of a tilted cylinder primarily arises from flow asymmetry induced by the angle of attack, three-dimensional vortex development, and the height-dependent characteristics of boundary layer separation, as Figure 10 shows. When a 60°attack angle is imposed, the flow field exhibits significant axial variations: the upstream region experiences earlier separation and enhanced velocity gradients due to angle dominance, while downstream regions (away from the top) show amplified turbulent fluctuations from developing three-dimensional structures. Along the cylinder's height, boundary layer separation locations and thicknesses vary, with upper cross-sections exhibiting earlier separation under pronounced attack effects, whereas lower sections display localized velocity gradient discrepancies due to stabilized flow fields and three-dimensional vortex-induced mixing. The vortex street's core positions and shedding frequencies also vary with height, where mid-sections present quasi-two-dimensional vortex street patterns, while top/bottom sections develop non-uniform velocity distributions due to intensified three-dimensional disturbances. Additionally, vertically varying pressure gradients caused by the angle of attack lead to differing interaction intensities between the mainstream flow and wake vortices at different heights.

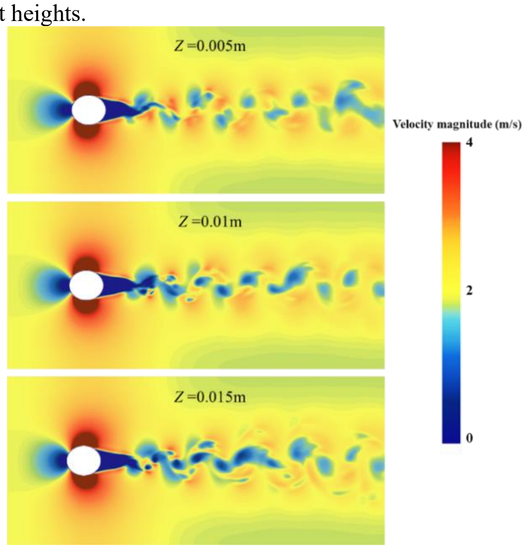

Fig. 10 Velocity contour plots at different *z* cross-sections of a 60°-inclined cylinder.

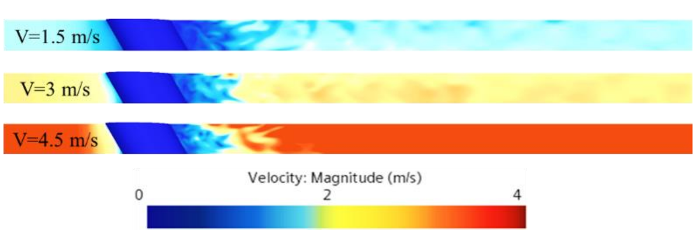

Fig. 11 Longitudinal cross-sectional velocity contour of a 60°-inclined cylinder.

The cross-sectional velocity contour is shown in Figure 11. The velocity distribution in the wake region of cylinders of identical size under different freestream velocities differs due to variations in the Reynolds number, which governs transitions in flow regimes, vortex structures, and energy dissipation mechanisms. At low velocities, the wake exhibits symmetric, periodic von Kármán street patterns with stable velocity profiles, where vortex shedding frequencies linearly correlate with the Strouhal number. As velocity increases, the separation point shifts upstream, three-dimensional vortex structures intensify, and turbulent kinetic energy in the wake significantly increases, leading to amplified velocity fluctuations and heightened asymmetry in the distribution. The wake evolves into complex vortex clusters with strong vortex-vortex interactions. This disparity fundamentally stems from the balance between inertial and viscous forces regulated by Re: at low Re, viscous effects dominate, maintaining ordered flow; at high Re, inertial forces drive turbulent pulsations and stochastic three-dimensional activities, resulting in enhanced spatial heterogeneity and temporal variability in the wake velocity field.

CONCLUSIONS

Based on the study's findings, the maximum fluctuating pressure occurs at the cylinder separation point, with significant peaks also observed in the upstream and downstream directions. Larger cylinder diameters correspond to broader vorticity distribution ranges, which accounts for the increased overall pressure levels.

Higher incoming velocities result in larger vortex scales and enhanced energy levels. For fluctuating pressure spectra, increasing flow velocity leads to a rise in peak frequency and an elevation in the amplitude of the first-order peak, consistent with theoretical and experiment results.

Velocity contour plots at three elevations (z = 0.005 m, 0.01 m, and 0.015 m) for the inclined cylinder exhibit discrepancies, indicating vertical-dependent flow field variations along the cylinder's height. These differences would influence pressure fluctuations.

This paper, as the first part of a numerical study on fluctuating pressure for slender cylindrical bodies, begins with a simplified problem formulation, without considering six-degree-of-freedom motion or the presence of waves. Future work may incorporate the influence of these factors.

REFERENCES

Karthik K, Jeyakumar S, Sarathkumar SJ (2020). "Numerical prediction of flow noise levels on towed sonar array," *Journal of Engineering for the Maritime Environment*, 20.

Sean M (2019). "Towed array sonar: uses and design challenges," *Newport: Engineered Interconnect and Packaging*, 2.

Stephen AJ (2014). "Understanding tow tank measurements of total drag for long thin circular cylinders," *Journal of Fluids Engineering*, 136 (031205):1-8.

Tutty OR (2008). "Flow along a long thin cylinder," *Journal of Fluid Mechanics*, 602: 1–37.

Yu LJ, Zhao WW, Wan DC (2021). "Propeller Wake and Noise Analysis Based on the Third-Generation Vortex," *Liutex and Third Generation of Vortex Identification: Workshop from Aerospace and Aeronautics World Forum 2021*. Singapore: Springer Nature Singapore, 257-270.